CHEMPHYSCHEM

DOI: 10.1002/cphc.200500613

Water Formation on Pt and Pt-based Alloys: A Theoretical Description of a Catalytic Reaction

Timo Jacob*[a] and William A. Goddard III[b]

In the past, the modeling of catalytic processes was limited by the size and complexity of the systems involved. However, the enormous progress in both computer power and theoretical methods has made computational modeling a valuable tool in increasing our knowledge of catalytic reactions on the atomic scale. While complex reactions can be studied by dividing the overall reaction into a series of steps calculable by quantum mechanics, the combination with methods appropriate for larger time and length scales enables the gap between these regimes to be bridged. This provides a more realistic modeling of the experimental system and allows important environmental effects such as solvation to be taken into account. In this Minireview we describe some of the main theoretical methodologies that are used to study catalytic properties and reactions on surfaces. Using these methods, we study the seemingly simple reaction of water formation out of hydrogen and oxygen on Pt and Pt/Ni alloy catalysts. To provide a more realistic description we also discuss the interesting effects determined by hydrating the system or using alloy nanoparticles rather than extended surfaces.

1. Introduction

Historically, surface catalysis dates back to the early 1800s, when Döbereiner discovered the Pt-surface-catalyzed reaction of H_2 and O_2. Since then an enormous scientific effort has helped the understanding of catalytic reactions and the discovery of new catalyst materials. As a result, nowadays catalysis plays a tremendous role in the industrial production of an innumerable variety of different compounds ranging from polymers to pharmaceuticals and petrochemicals.

In catalytic reactions certain bonds of the educts are broken and others are formed, finally resulting in the desired product. Without catalyst these reactions would either run with low efficiency (or lower rates) or even not occur, and therefore it is the role of the catalyst to lower the barriers involved in certain bond breakings and thus increase the efficiency. For multistep reactions, in which only a particular reaction mechanism is desired, the catalyst also has to prevent unwanted reactions from occurring.

To understand the relevant surface properties that lead to a particular catalytic process, experimental and theoretical techniques had to be developed to characterize catalytic surfaces as well as to study surface phenomena, such as adsorption, diffusion, rearrangement, nucleation, charge transfer, or reactions. A variety of different experimental approaches have been evolved to obtain surface information on the atomic scale,[1] and the formulation of quantum mechanics in the 1920s provided the theory for understanding the electronic structure. Since then the main aim of theoretical modeling has been (and still is) the development of methods or approximations that enable the many-body Schrödinger equation to be solved for a particular system. Knowledge of the electronic structure reveals information necessary to interpret catalytic reactions and to deduce many important system properties, such as preferred structures, transition states, vibration frequencies, or related thermodynamic potentials. This finally enables theory to characterize catalytic surfaces by finding reactive surface sites important for catalysis, to distinguish between possible reaction pathways, or to understand changes in the reactant behavior during surface reactions.

Besides homogeneous metal surfaces, metal alloys open another wide field for catalyst improvement. By mixing two metals that by themselves might have similar properties, a material with completely different characteristics could be formed. Consequently, the bulk and surface geometries might be different, which could lead to rough surfaces dominated by relaxations, reconstructions, or segregations.[2] These effects, in addition to the alloying, result in a modified electronic structure of the surface. For instance, by alloying Pt with Ru a catalyst can be formed whose site selectivity results in surfaces that are more resistant to CO adsorption.[3]

Another way to improve the efficiency of a catalytic process is to use highly dispersed particles rather than extended surfaces. This provides an overall larger reactive surface area at which the catalytic reactions could occur simultaneously. However, the use of nanoparticles again introduces new properties, such as quantum size effects for small particle sizes or polymorphic particle shapes.[4,5] In addition, the overall catalyst surface is generated by different surface faces connected via step

[a] *Dr. T. Jacob*
Fritz-Haber Institut der Max-Planck Gesellschaft
Faradayweg 4–6, 14195 Berlin (Germany)
Fax: (+49) 30-8431-4701
E-mail: jacob@fhi-berlin.mpg.de

[b] *Prof. Dr. W. A. Goddard III*
Materials and Process Simulation Center, Beckman Institute (139-74)
California Institute of Technology
Pasadena, CA 91125 (USA)

edges or kinks, all of which usually show different catalytic reactivities. Thus, experimentally measured reactivities of nanoparticles are influenced by these effects.

For the theoretical modeling of catalytic reactions on alloys or with nanoparticles this means another level of complexity. Before the actual reaction can be studied, careful and time-consuming investigations on the structure, shape, and/or composition of the catalyst surface are necessary. This ensures that the same catalyst underlies both the experiment and the theoretical model, allowing a reliable comparison.

Herein, we will first describe some of the major methods that are used to study catalytic reactions on surfaces (Section 2). Possible approaches to choosing an appropriate surface model are discussed (Section 3) and applied in a comprehensive study of water formation on Pt(111) (Section 4), where additional effects are successively taken into account. In Section 5 we describe the changes in the surface structure due to alloying Pt with Ni (or Co) and discuss their relevance for alloy nanoparticles. In the latter case we finally show the changes for OH formation, a relevant reaction step in water formation.

2. Methods

Catalytic reactions on surfaces usually involve changes in the system geometry and electronic structure of the interacting compounds. Thus, modeling catalysis requires methods on the atomic scale which accurately describe the effects determined by quantum mechanics. Here, density functional theory (DFT) has become a powerful tool that has widely proven its applicability to metals, semiconductors, and insulators. However, DFT is still only able to handle rather small system sizes (around <100 atoms) and short timescales (femtoseconds) compared to realistic systems in surface catalysis, and so the simulation of more extended systems or longer time evolutions requires additional approximations. By parameterizing experimentally or theoretically obtained system properties, force fields try to bridge the gap to larger time and length scales due to an analytically formulated Hamiltonian. However, the applicability of a particular force field to different problems strongly depends on the form of the energy expression, but more importantly on the quality of the parameterization.

If the interest is in accurately describing only a certain part of the system that is relevant for a catalytic reaction (e.g. by DFT), but also including the influence of an environment (e.g. solvation), then the surrounding can be modeled either by a lower level of theory or as a continuum. The first approach takes the environmental atoms or molecules explicitly into account, while the latter method applies a so-called implicit treatment.

2.1. Density Functional Theory

To study catalytic processes, a detailed knowledge of the electronic structure of a system is required. Although in principle this can be obtained by solving the many-body Schrödinger equation, approximations have to be made for systems beyond the hydrogen molecule. Besides wave-function-based (or Hartree–Fock)[6,7] approximations, DFT has become one of the dominant approaches in electronic structure calculations. It provides a good balance between efficiency and accuracy for various systems in heterogeneous and homogeneous catalysis.

The basis of DFT is given by two theorems formulated by Hohenberg and Kohn,[8] which state that the total energy of a system in its ground state only depends on the electron density ($E=E[\rho]$), and provide a variational principle (for a given energy functional) to evaluate this density ($\delta_\rho E[\rho]=0$). Although the existence of such an energy functional was proven, the exact form still remains unknown. Important for the practical use of DFT was a reformulation by Kohn and Sham[9] that divided the energy functional into three parts: kinetic energy, Coulomb energy ($E_{e\text{-}e}+E_{e\text{-}n}+E_{n\text{-}n}$), and the exchange-correlation (xc) energy as shown in Equation (1):

$$E[\rho] = T_s[\rho] + E_{\text{Coulomb}} + E_{xc}[\rho] \tag{1}$$

where $T_s[\rho]$ is the kinetic energy of a system containing noninteracting electrons (given by density ρ) and $E_{xc}[\rho]$ accounts for exchange and correlation energy of the interacting system.

If the electron density is now represented by one-particle wave functions (Kohn–Sham orbitals) [Eq. (2)]:

$$\rho(\mathbf{r}) = \sum_i n_i |\psi_i(\mathbf{r})|^2 \tag{2}$$

then performing the variation of the energy functional leads to the Kohn–Sham equations, which can be solved self-consistently [Eq. (3)]:

$$\left[-\frac{\hbar}{2m}\nabla^2 + V_{\text{eff}}(\mathbf{r}) + V_{xc}(\mathbf{r})\right]\psi_i(\mathbf{r}) = \varepsilon_i\psi_i(\mathbf{r}) \tag{3}$$

with an effective and an exchange-correlation potential given by Equation (4):

$$V_{\text{eff}}(\mathbf{r}) = V^{\text{ext}}(\mathbf{r}) + \int \frac{\rho(\mathbf{r}')}{|\mathbf{r}-\mathbf{r}'|}\mathrm{d}^3\mathrm{r}' \text{ and } V_{xc}[\rho(\mathbf{r})] = \frac{\delta E_{xc}[\rho(\mathbf{r})]}{\delta\rho(\mathbf{r})} \tag{4}$$

Since the exact exchange-correlation functional is still unknown, different attempts exist to approximate this functional. The simplest approximation is known as the local density approximation (LDA) [Eq. (5)]:[9]

$$E_{xc}^{\text{LDA}}[\rho(\mathbf{r})] = \int \varepsilon_{xc}[\rho(\mathbf{r})]\rho(\mathbf{r})\mathrm{d}^3\mathrm{r} \tag{5}$$

where $\varepsilon_{xc}[\rho(\mathbf{r})]$ is the xc-energy per electron of a homogeneous electron gas. This type of functional was found to reproduce bond distances for a variety of systems, but usually overestimates binding energies.[10]

Another group of functionals, known under the generalized gradient approximation (GGA), try to account for the inhomogeneous character of the density [Eq. (6)]:

$$E_{xc}^{\text{GGA}}[\rho(\mathbf{r}), \nabla\rho(\mathbf{r})] = \int f[\rho(\mathbf{r}), \nabla\rho(\mathbf{r})]\rho(\mathbf{r})\mathrm{d}^3\mathrm{r} \tag{6}$$

where $f[\rho(\mathbf{r}),\nabla ?(\mathbf{r})]$ also depends on the gradient of ρ. Compared to LDA this type of functional usually better reproduces the energetics (e.g. binding energies or barriers).[11] For further information on commonly used functionals of this type, we refer the reader to ref. [12].

We would also like to mention the so-called hybrid functionals that combine exact Hartree–Fock exchange with contributions from local and nonlocal functionals (e.g. B3LYP[13,14]). These functionals are commonly used in quantum chemistry to study organic compounds. Finally, it should be remarked that the Kohn–Sham equations can also be generalized for spin-polarized systems by distinguishing different spin directions.

2.2. Force Field Methods

Describing systems quantum-mechanically from first principles is, due to the required computational resources, still limited to sizes typically of a hundred atoms. Although this already allows the study of many different problems in heterogeneous and homogeneous catalysis, other techniques are desirable that enable larger molecules or surfaces with reduced symmetry to be treated without losing too much accuracy. Besides various semiempirical approaches, which will not be discussed here, modern ab initio force fields[15–18] are able to provide reasonably accurate energetics and structures. In those force fields the system energy is divided into several terms, which account for different types of interactions as indicated in Equation (7):

$$E_{\text{System}} = E_{\text{Bond}} + E_{\text{Angle}} + E_{\text{Torsion}} + E_{\text{Coulomb}} + E_{\text{vdW}} + \ldots \quad (7)$$

As each term is given by an analytic expression the system energy can be evaluated rather quickly, which allows the dynamics of extended systems to be simulated on the nanosecond scale. However, since every energy term is parameter-dependent, the quality and accuracy of a particular force field strongly depends on these parameters, which are usually obtained by fitting to system properties either measured experimentally or calculated with a higher level of theory (e.g. DFT). Notably, adapting force field parameters to a particular set of systems (e.g. small molecules) does not imply general transferability of the force field to another set of systems (e.g. extended surfaces).

Besides nonreactive force fields as described above, which require an explicit definition of which atoms interact with each other by a certain type of interaction (usually given by a bonding table), there is the class of reactive force fields[19–21] that are also capable of describing reactions. Although the basis of reactive force fields is a system energy expression comparable to Equation (7), each term is explicitly bond-order dependent. By taking the electronic configuration of each atom type into account and continuously mapping the local environment of an atom during a simulation, the bond order is updated and thus certain interaction terms might vanish (bond breaking) or appear (bond formation). Therefore, the different energy terms of Equation (7) can no longer be categorized in *n*-body terms, but each has multibody character. In addition, by including further energy terms these force fields become able to distinguish between variations in structure and energy of differently hybridized organic compounds. For example, this plays an important role in reactions with hydrocarbons or Si.[22] Recently, reactive force fields have also been applied to studying the energetics of reactions on transition-metal surfaces.[23]

2.3. Solvation

Most chemical and biochemical processes occur in the condensed phase rather than in gas phase. However, to include solvation effects in electronic structure calculations implies more complex systems. The main methods used for theoretical modeling can basically be categorized into two main approaches: the explicit and the implicit treatments.

The explicit solvent model (an overview can be found in refs. [24,25]) describes the solvent by individual molecules, which are mostly treated with the same level of theory. Although this model is capable of reproducing the detailed structure of the solute/solvent interface for systems near equilibrium and along reaction pathways (for example, Car–Parrinello ab initio molecular dynamics (CPMD)[26]), in a purely quantum-mechanical treatment the system size is limited by the computational expense, and thus is restricted to a relatively small number of solvent molecules. Therefore, in an alternative approach the entire or at least parts of the solvent are treated with a lower level of theory than the solute, for example, by molecular mechanics.[24,25,27–29] Within these methods, known as QM/MM, the solvent–solvent and solute–solvent interactions are mostly given by a sum of electrostatic and van der Waals contributions. While the van der Waals interactions are often evaluated by Lennard–Jones-type potential functions,[27,28,30] an appropriate handling of the electrostatic interactions between solute and solvent, which couples the quantum-mechanically treated solute with the molecular-mechanically treated solvent, is important. Approaches for this contribution are based, for example, on a multipolar expansion of the QM wave functions[31,32] or a solvent-averaged potential.

In implicit solvent models[33,34] the solvent is replaced by a continuum with an appropriate dielectric constant. The solute is then placed in a cavity, whose size and shape have to be chosen properly. In many continuum approaches atom-centered interlocked spheres of certain radii[33,35] (e.g. van der Waals radii), or the solvent-excluded surface (SES)[36] or solvent-accessible surface (SAS),[37] are used to define this cavity. Due to electrostatic interactions the solute polarizes the solvent, which then forms a reaction field that couples back to the solute. The corresponding electrostatic potential, which is required to evaluate the interaction energy, is obtained by solving the Poisson–Boltzmann equation (assuming a Boltzmann-type distribution of ions within the solvent). This leads to a solvation free energy given by Equation (8):

$$\Delta G^{\text{sol}} = \Delta G^{\text{chg}} + \Delta G^{\text{cav}} \quad (8)$$

where ΔG^{cav} is the free energy to create the cavity and ΔG^{chg} accounts for charging the solvent near the solute.

In quantum-mechanical calculations of a solute electronic structure, the solvent reaction field is incorporated in the self-consistency cycle, which leads to the so-called self-consistent reaction field approach (SCRF). Instead of expensively solving the Poisson–Boltzmann equation directly, different approximations exist which can evaluate the solvation free energy by analytic expressions, for example, the generalized Born model,[38,39] Bell model, or Onsager model.[33,34]

3. Surface Model

To study surface-specific problems, such as structures, adsorptions, or even catalytic reactions, much care has to be taken to determine an appropriate surface model. Here, one can distinguish between two major approaches: the slab/supercell approach and the cluster approximation. Both models have advantages and disadvantages, which is why the choice depends on the particular physical or chemical question to be answered.

Within the slab/supercell approach the two-dimensional (2D) translation symmetry of a surface is used to reduce the calculation to a single unit cell (Figure 1). The surface is modeled by a slab of finite thickness due to the application of periodic boundary conditions (PBCs), which introduce the semi-infinite character of the system. However, to avoid nonphysical interaction between both surfaces on the top and the bottom, the slab has to be chosen thick enough such that its center reproduces bulklike behavior. Depending on the system this requires between five and 20 atomic layers. Semiconductors and certain transition metals already exhibit major surface properties, such as surface states or adsorbate binding energies with five-layer slabs, but some simple metals (e.g. Al) require more extended slabs.[40] In addition, since each slab interacts with its virtual copies above and beneath, a sufficiently large vacuum spacing is necessary to minimize these effects. If the interest is in studying catalytic reactions on surfaces, the 2D unit cell must also be chosen large enough such that the adsorbed species in one cell do not see their images in adjacent cells. Besides these direct interactions, neighboring adsorbates may also indirectly interact through changes in the electronic structure of the surface. For illustration the graph in Figure 1 shows the DFT-calculated binding energy of a single oxygen atom (with respect to half an O_2 molecule) to an fcc site of a Pt(111) slab as a function of unit-cell size (or coverage). The calculations were performed with SeqQuest[41,42] employing the GGA-type exchange-correlation functional suggested by Perdew, Burke, and Ernzerhof (PBE).[43] Until a coverage of 0.11 monolayers (MLs) is reached, which can be achieved with a 3×3 unit cell, there are non-negligible direct and/or indirect interactions.

The second method is the cluster approximation, in which the system is represented by a finite part of the surface (see Figure 2). By using such a finite system to study surface adsorptions or reactions one avoids most problems connected with the slab approach, but this method has to deal with other crucial aspects. In particular, if the aim is to model metallic surfaces, then with small clusters most (or even all) atoms are surface atoms, which cause unwanted border effects and an unpredictable behavior of the cluster. As an example, the right-hand graph in Figure 2 shows the binding energy of atomic oxygen (again with gas-phase O_2 as reference) to the (111) plane of differently sized and shaped Pt clusters, which was obtained with DFT using the B3LYP[13,14] xc-functional and a LACVP** basis set (see ref. [44] for further information). With less than 20 atoms the binding energy is strongly system-dependent and even the preferred adsorption site alternates. Ex-

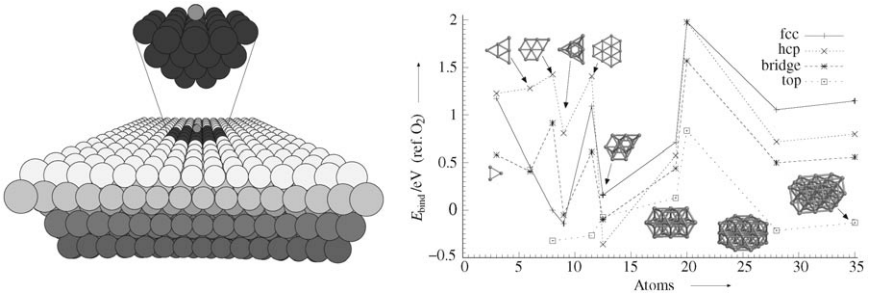

Figure 2. Left: In the cluster approach a well-defined, finite cluster is used to model the surface. Right: Binding energies (with respect to gas-phase O_2) of atomic oxygen on differently sized and shaped clusters (Pt_3, Pt_6, Pt_8, Pt_{12}, $Pt_{6.3}$, $Pt_{12.8}$, $Pt_{5.10.5}$, $Pt_{9.10.9}$, $Pt_{14.13.8}$). For each cluster the binding energies at face-centered cubic (fcc), hexagonal close packed (hcp), bridge, and on-top sites are given.

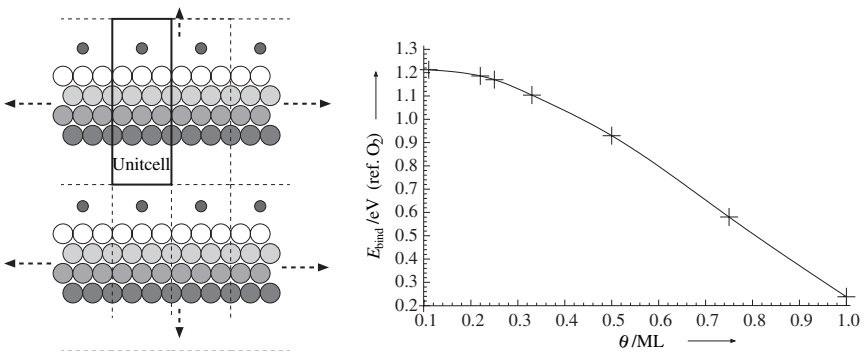

Figure 1. Left: Illustration of the supercell approach for surface calculations. The periodically repeated unit cell (slab in 2D) has to be large enough to minimize interactions with neighboring unit cells. Right: Binding energy of an oxygen atom as a function of surface coverage (with gas-phase O_2 as reference).

tending the cluster to more than 20 atoms results in the same preferred adsorption site for oxygen and similar relative stabilities (ΔE_{bind}). However, convergence in both binding energy and adsorption structure requires systems with at least three layers and 28 atoms. The binding energies obtained with such extended systems agree quite well with those obtained on the basis of periodic slab calculations for low coverages. While this is valid for Pt clusters, surfaces of other metals might require more extended systems (for example, $\geq$56 atoms for Cu(100),[45] or >100 atoms for Al(100)[46]). Thus, although finite systems are able to mimic surfaces, careful studies on cluster-size convergence are necessary.

4. Water Formation on Pt(111)

The formation of water out of hydrogen and oxygen is one of the important reactions occurring in fuel cells. At the cathode four protons react with a dioxygen molecule with acceptance of four electrons to give two water molecules [Eq. (9)]:

$$O_2 + 4\,H^+ + 4\,e^- \rightarrow 2\,H_2O \qquad (9)$$

Although possible intermediates consist only of hydrogen and oxygen, there is still uncertainty about the exact reaction mechanism. As a realistic electrochemical system (such as a fuel cell) is from the theoretical point of view an extremely complex system, in which the catalytic reactions occur in a multicomponent environment and under conditions of finite temperature, pressure, and electrode potential, in the following we will discuss the idealized case of platinum-catalyzed hydrogen combustion in oxygen [Eq. (10)]:

$$H_2 + {}^1/_2\,O_2 \rightarrow H_2O \qquad (10)$$

which is quite interesting by itself,[47] but still far away from the realistic electrochemical system.

To study possible pathways for Equation (9), first all possible intermediates were considered separately: H, H_2, O, O_2, OH, OOH, H_2O_2, and H_2O. The stable surface sites and the binding energies on Pt(111) were evaluated for each intermediate, while the surface was modeled by a 35-atom three-layer cluster (Pt_{35}), which gave cluster-size-converged results. Pt_{35} consists of 14 atoms in the first layer, 13 in the second, and 8 atoms in the third layer. Then different dissociation processes of the adsorbed molecules were studied to obtain the energetic barriers involved. Here it should be remarked that to find the transition states only the single distance between the dissociation products has been constrained, while the remaining system was allowed to freely optimize its structure. In addition, the transition state obtained was checked by analyzing the vibrational spectra. Thus, by using the energetics and dissociation barriers we can draw a picture of different pathways for the gas-phase reaction and show their corresponding rate-limiting steps. For a detailed description of the adsorption and dissociation processes including energetic and structural information on each intermediate, which would very much extend the scope of this review, see ref. [48]. This work also includes a detailed comparison with available experimental results and other calculations.

In general, two major pathways can be distinguished. First, the O_2 dissociation pathway that involves the dissociation of dioxygen as one of the first reaction steps to generate two oxygen atoms on the surface, which then can react with adsorbed H atoms to form water. The second route is the OOH formation pathway, in which the O_2 molecule is not dissociated directly but reacts with hydrogen to form OOH or H_2O_2, which then dissociates. In the following we will discuss the reaction mechanisms in more detail without and including zero-point energy (ZPE) corrections, and will then point out the changes expected by hydrating the system.

4.1. O_2 Dissociation Pathway

The reaction mechanisms involving direct O_2 dissociation are combined in Figure 3. According to the motivation given above, we start with molecular H_2 and O_2 in the gas phase (not adsorbed) and the plain Pt surface (Pt_{35} cluster). The heat of formation (ΔH_f) of this system is set to zero. For reaction to occur we first adsorb H_2 on the surface, which undergoes barrierless dissociation.[49] This lowers the energy of the whole system by 0.63 eV, which is two times the binding energy (BE) of atomic hydrogen (2.73 eV) minus the dissociation energy of gas-phase H_2 (calculated with the B3LYP functional to be 4.84 eV). Since hydrogen has a low diffusion barrier of approximately 0.05 eV[50] on Pt(111), we assume hydrogen to always be present on the surface for further reactions.

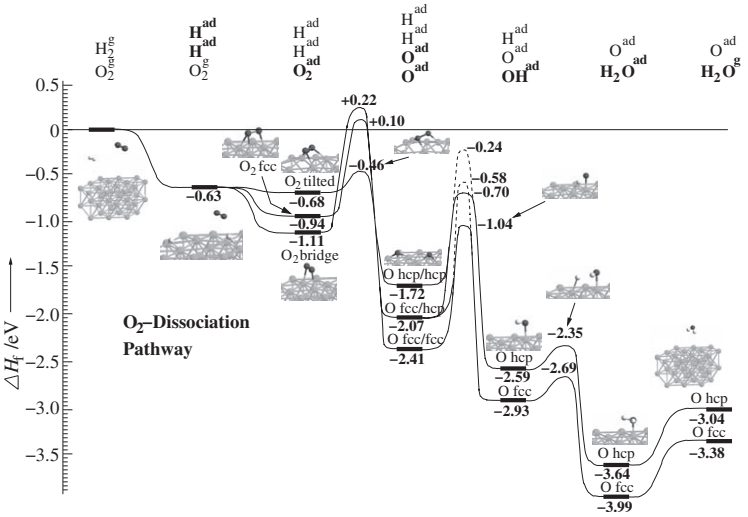

Figure 3. Heats of formation for the O_2 dissociation pathway (without ZPE corrections). The reference ($\Delta H_f = 0$ eV) is the bare Pt_{35} cluster plus separated H_2 and O_2 molecules in the gas phase. Multiple structures are possible for some adsorbed systems, and thus there is splitting of the ΔH_f values. In these cases the label below the value indicates the specific part of the system.

Then O_2 adsorbs molecularly, for which we can distinguish three, stable binding geometries: bridge (BE = 0.49 eV), fcc (BE = 0.31 eV), and tilted (BE = 0.06 eV). In the most stable configuration O_2 is bound on a bridge position, where both oxygen atoms use a doubly occupied p orbital to form weak surface bonds. With two hydrogen atoms and an O_2 molecule now on the surface, in this reaction pathway the next step is dissociation of dioxygen. However, for each of the adsorbed O_2 structures we obtain a different dissociation barrier. At the bridge position this barrier is highest (1.33 eV), followed by the fcc position (1.04 eV). The lowest barrier we obtain is for tilted O_2 (0.22 eV), whose initial structure is comparable to bridge-bound O_2 but tilted toward the surface such that the O=O double bond is able to form a donor–acceptor bond to an adjacent Pt atom. Although O_2 is most likely to bind at a bridge surface site, the difference to the tilted configuration is 0.90 eV lower than the bridge site dissociation barrier. Thus, O_2 may undergo a structural change toward the O_2 tilted configuration while dissociating, which agrees with the calculations of Eichler et al.[51] This would drastically lower the overall dissociation barrier from 1.33 to 0.65 eV, which much better agrees with the 0.38 eV measured by STM.[52] In either case, the final system contains two adsorbed oxygen atoms located in threefold sites: O_{hcp}/O_{hcp}, O_{fcc}/O_{hcp}, or O_{fcc}/O_{fcc}.

Notably, dissociation of O_2 in any configuration leads to two oxygen atoms in nonadjacent threefold positions (separated by two lattice constants), which is in excellent agreement with the STM experiments by Ho.[53,54] For the case in which dissociation of multiple O_2 molecules occurs at different surface positions, the final structure will thus correspond to a p(2×2) overlayer, exactly what is observed experimentally.[55] In addition, this result allows us to treat both oxygen atoms as nearly independent adsorbates (see Figure 1). Therefore, we will neglect the remaining O–O interaction of both dissociation fragments. However, for completeness both possible adsorption sites (O_{hcp} or O_{fcc}) of the second O atom are considered in Figure 3 without having influence on further reaction barriers. Since the barrier to hop from an hcp to an fcc site via a bridge position is only 0.24 eV, we expect most atomic oxygen to equilibrate to fcc sites after a finite time.

The next reaction step is OH formation, which involves a barrier of 1.37 eV. In contrast to the dissociation of O_2, there is no possible trajectory to lower the formation barrier by using parts of the energy to change the adsorption site. The dashed lines in Figure 3 indicate a less likely configuration (higher in energy), in which hydrogen and oxygen do not approach along a Pt–Pt bridge direction, but via a threefold site (see ref. [48] for further information). However, since there may always be structural fluctuations caused by surface vibrations, only the lower-energy process in which the H atom approached along the Pt–Pt bridge direction should be relevant. Finally, this leads to adsorbed H (mobile), fcc-bound O (partially hcp-bound), and OH.

Within both final steps the water molecule is created on the surface and desorbs to give gas-phase water, the final product of the reaction. Since both water and OH adsorb on Pt(111) with the oxygen at an on-top surface site, the reaction of forming water out of adsorbed H and OH is determined by the energy difference of changing the Pt–OH covalent bond (2.06 eV) into a bond of the oxygen lone-pair orbital (0.60 eV), breaking the Pt–H bond (2.73 eV), and forming the additional O–H bond (5.25 eV), which leads to the derivation of Equation (11):

$$\begin{aligned}&\Delta H_f(H^{ad} + OH^{ad}) - \Delta H_f(H_2O^{ad})\\ &= BE(HO{-}H) + BE(Pt{-}H_2O) - BE(Pt{-}OH) - BE(Pt{-}H) \qquad (11)\\ &= 5.24 + 0.60 - 2.06 - 2.73 = 1.06\ eV\end{aligned}$$

The barrier for this formation is 0.24 eV. Finally, to desorb water from the surface we have to break the Pt–H_2O surface bond. The energy required for this process is 0.60 eV, which can be compared to an experimental value of 0.52 eV.[56]

Assuming the reaction mechanism with the lowest barrier for each reaction step, we can finally draw the following picture of the whole O_2 dissociation pathway (upper numbers are changes in heat of formation ΔH_f, and lower, bold numbers indicate the energetic barrier of the corresponding step), where all energies are given in eV [Eq. (12):

$$\begin{aligned}&H_2{}^g + O_2{}^g \xrightarrow{-0.63} 2\,H^{ad} + O_2{}^g \xrightarrow{-0.48} 2\,H^{ad} + O_2{}^{ad}\\ &\xrightarrow[\mathbf{0.65}]{-1.30} 2\,H^{ad} + 2\,O^{ad}{}_{fcc} \xrightarrow[\mathbf{1.37}]{-0.52} H^{ad} + OH^{ad} + O^{ad}{}_{fcc} \qquad (12)\\ &\xrightarrow[\mathbf{0.24}]{-1.06} H_2O^{ad} + O^{ad}{}_{fcc} \xrightarrow{+0.61} H_2O^g + O^{ad}{}_{fcc}\end{aligned}$$

Comparison of the heats of formation shows that all reaction steps are exothermic except the last step of desorbing water from the surface. Overall, starting with $H_2{}^g$ and $O_2{}^g$ the whole system gains 3.38 eV while reacting to form H_2O^g and fcc-adsorbed atomic oxygen. Subtracting $\Delta H_f(O^{ad}{}_{fcc})$ from the overall energy gain gives 3.38 − 0.89 = 2.49 eV, which is in good agreement with the tabulated enthalpy value of 2.51 eV for the reaction $H_2{}^g + {}^1/_2\,O_2{}^g \rightarrow H_2O^g$.

Along the reaction pathway there are only three steps that include barriers. The highest barrier is the $O^{ad}{}_{fcc} + H^{ad} \rightarrow OH^{ad}$ reaction with 1.37 eV. The dissociation of adsorbed $O_2{}^{ad}$, which is mostly considered to be the limiting process,[57] has a 0.72 eV lower activation barrier. The third reaction step involving a barrier is the formation of water on the surface out of OH^{ad} and H^{ad}. However, the energy required is only 0.24 eV. Comparing these values with the reaction steps in the gas phase shows that the Pt surface lowers the O_2 dissociation barrier from 4.95 eV in the gas phase to only 0.65 eV. In addition, on the Pt catalyst the rate-determining step is not the O_2 dissociation (as for the gas-phase reaction), but the formation of OH.

If we now consider zero-point energy corrections, the overall energetics changes slightly as shown in Equation (13):

$$\begin{aligned}&H_2{}^g + O_2 \xrightarrow{-0.32} 2\,H^{ad} + O_2{}^g \xrightarrow{-0.33} 2\,H^{ad} + O_2{}^{ad}\\ &\xrightarrow[\mathbf{0.63}]{-1.25} 2\,H^{ad} + 2\,O^{ad}{}_{fcc} \xrightarrow[\mathbf{1.13}]{-0.58} H^{ad} + OH^{ad} + O^{ad}{}_{fcc} \qquad (13)\\ &\xrightarrow[\mathbf{0.09}]{-1.05} H_2O^{ad} + O^{ad}{}_{fcc} \xrightarrow{+0.42} H_2O^g + O^{ad}{}_{fcc}\end{aligned}$$

The Pt cluster has a much larger mass than each of the gas-

phase compounds, and therefore by including zero-point energy corrections major changes occur with reaction steps where atoms or molecules adsorb onto or desorb from the surface. For instance, by dissociatively adsorbing gas-phase H_2 the system gains 0.31 eV less energy than when zero-point energy corrections are not considered. In addition, as adsorbed hydrogen shows strong vertical vibrations (on top: 2456 cm^{-1}; threefold: 1317 cm^{-1}),[50,58] reactions that use H^{ad} (e.g., $O^{ad}_{fcc} + H^{ad} \rightarrow OH^{ad}$) now have $\approx$0.20 eV lower energy barriers. However, besides these slight changes the formation of OH^{ad} still has the highest energy barrier at 1.13 eV.

4.2. OOH Formation Pathway

The second possible reaction pathway includes OOH as an intermediate (see Figure 4). Instead of first dissociating $O_2{}^{ad}$ and then adding hydrogen atoms to form water, in this pathway $O_2{}^{ad}$ first reacts with a hydrogen atom on the surface and afterwards undergoes dissociation to form adsorbed H and OH.

Again we start with molecular $O_2{}^g$ and $H_2{}^g$, and the plain Pt surface. After adsorption of $O_2{}^g$ and dissociative adsorption of $H_2{}^g$, we again have two mobile hydrogen atoms and molecular oxygen, preferably in the bridge-bound configuration on the surface. The next reaction step is OOH formation. We have to consider different mechanisms of OOH formation because of the high mobility of an H atom on the Pt(111) surface. The first possibility is that the H atom could approach the O_2 molecule sideways (almost perpendicular to the O–O direction) and bind to one of the O atoms almost parallel to the surface. Due to the electronic rearrangement caused by the relatively strong O–H bond, the other O atom forms a covalent surface bond and the strong O=O double bond reduces to a single covalent bond (no-ring OOH^{ad}). The barrier for this whole process is 0.42 eV. However, when the H atom approaches the O_2 molecule along the Pt–Pt bridge direction, another stable OOH structure is created, in which OOH forms a five-membered ring with two surface Pt atoms. Due to the relatively strong Pt–H interaction that is established, the adjacent Pt–O connection (lone-pair bonding) becomes weaker, which finally results in a 0.38 eV lower barrier for the $O_2{}^{ad} + H^{ad} \rightarrow OOH^{ad}$ formation reaction. The resulting ring structure is relatively unstable and changes to the no-ring OOH^{ad} structure under only little perturbation. Therefore, further considerations use this OOH^{ad} structure.

The next step is the O–OH dissociation with a barrier of 0.74 eV. The products of this dissociation process are on-top bound OH^{ad} and O^{ad} at a threefold surface site. Since the O–OH dissociation is along the O–O direction, during the procedure the single O atom is on top of a Pt atom before moving to its final threefold site. This process results in no preferred threefold site for the single O atom (fcc or hcp). As for the O_2 dissociation pathway, an O atom at an hcp position can easily equilibrate and hop over a bridge position (0.24 eV barrier) to the fcc site. Thus, we assume this O atom to be at an fcc position. Both final steps of this reaction pathway ($OH^{ad} + H^{ad} \rightarrow H_2O^{ad} \rightarrow H_2O^g$) are equal to those discussed for the O_2 dissociation pathway.

Assuming the reaction mechanism with the lowest barrier for each reaction step, we can finally draw the following picture of the whole OOH formation pathway (upper numbers are again changes in ΔH_f, and lower, bold numbers indicate the energetic barrier of the corresponding step) [Eq. (14)]:

$$H_2{}^g + O_2{}^g \xrightarrow{-0.63} 2\,H^{ad} + O_2{}^g \xrightarrow{-0.48} 2\,H^{ad} + O_2{}^{ad} \xrightarrow[\mathbf{0.04}]{-0.60} H^{ad} + OOH^{ad} \xrightarrow[\mathbf{0.74}]{-1.22} H^{ad} + OH^{ad} + O^{ad}{}_{fcc} \xrightarrow[\mathbf{0.24}]{-1.06} H_2O^{ad} + O^{ad}{}_{fcc} \xrightarrow{+0.61} H_2O^g + O^{ad}{}_{fcc} \quad (14)$$

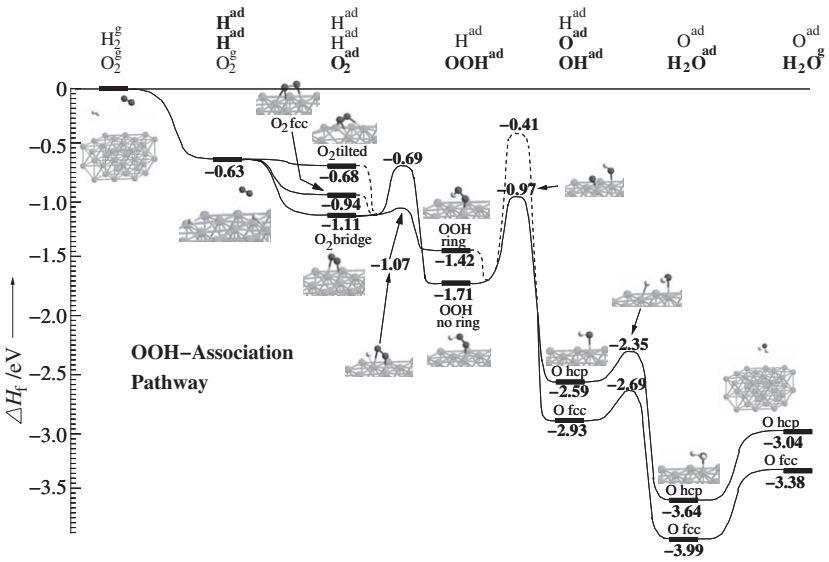

Figure 4. Heats of formation for the OOH formation pathway (without ZPE corrections). The reference ($\Delta H_f = 0$ eV) is the bare Pt_{35} cluster plus separated H_2 and O_2 molecules in the gas phase. Multiple structures are possible for some adsorbed systems, and thus there is splitting of the ΔH_f values. In these cases the label below the value indicates the specific part of the system.

Analogous to the O_2 dissociation pathway, only the last reaction step is endothermic by 0.61 eV. Since the remaining O atom may easily equilibrate to the fcc site, the system also gains a total 3.38 eV out of the whole reaction. The OOH formation pathway also involves three reaction steps with activation barriers: the reaction step to form OOH^{ad} out of $O_2{}^{ad}$ and H^{ad} (0.04 eV), the dissociation of an oxygen atom from OOH^{ad} (0.74 eV), and the final water formation out of OH^{ad} and H^{ad} (0.24 eV). Thus, the O–OH dissociation is rate-determining for the OOH formation pathway.

After including zero-point energy corrections, the reaction energetics changes as shown in Equation (15):

$$H_2{}^g + O_2{}^g \xrightarrow{-0.32} 2\,H^{ad} + O_2{}^g \xrightarrow{-0.33} 2\,H^{ad} + O_2{}^{ad}$$
$$\xrightarrow{-0.56} H^{ad} + OOH^{ad} \xrightarrow[\mathbf{0.67}]{-1.28} H^{ad} + OH^{ad} + O^{ad}{}_{fcc} \qquad (15)$$
$$\xrightarrow[\mathbf{0.09}]{-1.05} H_2O^{ad} + O^{ad}{}_{fcc} \xrightarrow{+0.42} H_2O^g + O^{ad}{}_{fcc}$$

As for the O_2 dissociation pathway shown in Equations (12) and (13), reaction steps that involve surface adsorption or desorption have lower ΔH_f values now, and reaction steps that use adsorbed hydrogen have slightly lower barriers. Since in Equation (14) the energy barrier for the formation of OOH^{ad} was already quite small (0.04 eV), it vanishes after inclusion of zero-point energy corrections. However, the O–OH dissociation still has the highest barrier at 0.67 eV.

Besides the OOH formation pathway described in Equations (14) and (15), it is also possible that adsorbed OOH does not dissociate directly, but first undergoes another hydrogenation step to form hydrogen peroxide (H_2O_2) on the surface. This reaction step has an energy barrier of 0.47 eV. Two OH^{ad} groups are then formed by dissociation of the O–O bond, which requires overcoming another energy barrier of only 0.29 eV. The intermediate reaction steps starting from hydrogen and OOH^{ad} can be written by Equation (16):

$$H^{ad} + OOH^{ad} \xrightarrow[\mathbf{0.47}]{-0.47} H_2O_2{}^{ad} \xrightarrow[\mathbf{0.29}]{-1.28} 2\,OH^{ad} \qquad (16)$$

Thus, by forming $H_2O_2{}^{ad}$ prior to O–O dissociation to OH^{ad}, the reaction step with the highest energy barrier is now the H_2O_2 formation, whose barrier is 0.20 eV below the rate-determining step in Equation (15).

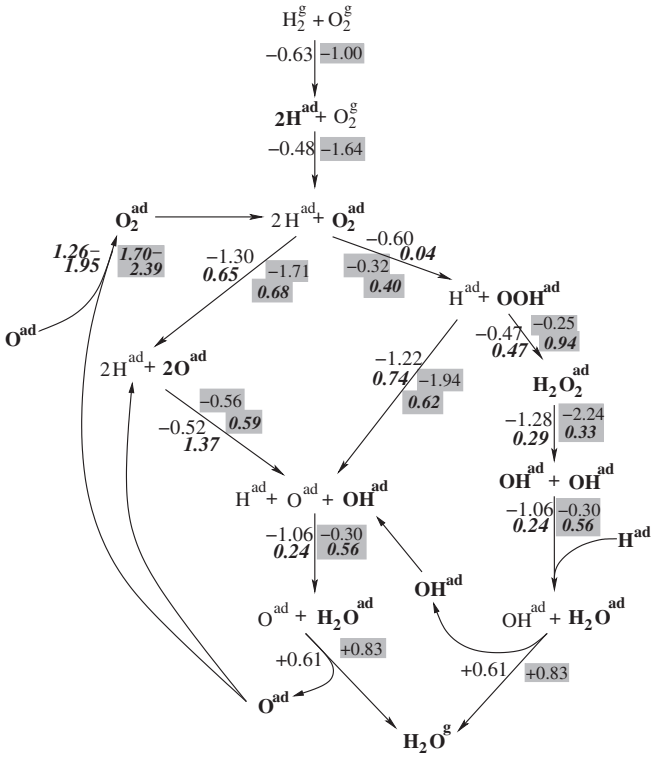

Figure 5. Scheme of all possible reaction pathways in the gas phase and when water solvated (highlighted numbers). Non-italic numbers give ΔH_f values for the particular reaction step, while bold italic numbers are the corresponding barriers (all values are in eV). In both cases the reference ($\Delta H_f = 0$ eV) is the bare Pt_{35} cluster plus separated H_2 and O_2 molecules in the gas phase or water solvent, respectively.

4.3. Overall Picture

An overall summary of the O_2 dissociation and OOH formation pathways (including $H_2O_2{}^{ad}$ as possible intermediate) is shown in Figure 5 as the nonhighlighted values. In addition, binding energies and dissociation barriers for all species before and after adsorption are given in Table 1 without and with consideration of zero-point energy correction. A comparison of the rate-determining steps of both reaction pathways shows a 0.66 eV lower barrier for the OOH formation pathway via $H_2O_2{}^{ad}$ over the O_2 dissociation pathway. Therefore, molecular H_2 and O_2 might rather take this OOH formation pathway to catalytically form the final product water. However, since the rate-limiting step of the OOH formation pathway via O–OH dissociation is only 0.20 eV higher than

Table 1. Binding energies and dissociation barriers for all studied molecules before and after adsorption on the Pt_{35} cluster. Energies before and after considering ZPE correction and for the water-solvated system are given. The adsorbate and the central four Pt atoms of the first layer (relaxation effects) were fully being geometry-optimized.

System	Adsorption site	E_{bind} [eV]			E_{diss} [eV]		
		No ZPE	With ZPE	Water solvent	No ZPE	With ZPE	Water solvent
H^g	–	–	–	–	–	–	–
O^g	–	–	–	–	–	–	–
$H_2{}^{g,aq}$	–	–	–	–	4.843	4.543	4.810
$O_2{}^{g,aq}$	–	–	–	–	4.974	4.902	5.461
$OH^{g,aq}$	–	–	–	–	4.568	4.313	4.832
$OOH^{g,aq}$	–	–	–	–	OO–H: 2.786	2.475	2.686
					O–OH: 3.168	3.041	3.315
$HOOH^{g,aq}$	–	–	–	–	H–OOH: 3.828	3.635	4.000
					HO–OH: 2.427	2.363	2.482
$H_2O^{g,aq}$	–	–	–	–	5.235	4.894	5.416
Pt_{35}–H	top	2.734	2.429	2.906	–	–	–
	bridge	2.641	2.478	2.567			
Pt_{35}–O	fcc	3.370	3.307	4.404	–	–	–
	hcp	3.026	2.960				
Pt_{35}–O_2	bridge	0.490	0.341	1.306	1.336	1.298	0.812
	fcc	0.313	0.174	1.638	1.035	1.002	1.105
	tilted	0.058	−0.072	0.849	0.219	0.217	−0.004
Pt_{35}–OH	top	2.057	1.907	3.033	1.895	1.720	2.048
Pt_{35}–OOH	no-ring	1.034	0.788	2.181	OO–H: 1.017	0.824	0.718
	ring	0.750	0.579	2.073	O–OH: 0.743	0.672	0.779
					OO–H: 0.359	0.258	0.813
Pt–HOOH	bridge	0.411	0.301	1.336	H–OOH: 0.946	0.732	1.191
					HO–OH: 0.291	0.183	0.330
Pt_{35}–H_2O	top	0.603	0.415	0.827	1.289	1.125	0.862

via $H_2O_2^{ad}$, it is quite likely that both OOH formation mechanisms play a certain role. Instead of using all educts the OOH formation pathway via O–OH dissociation produces atomic oxygen adsorbed on the surface without further usage. Thus, after a finite reaction time one might expect the surface to be covered with atomic oxygen. However, these O^{ad} atoms may partially drive the O_2 dissociation mechanism (and also react to form water) or recombine to give adsorbed dioxygen. Due to the strong surface bond of atomic oxygen to the Pt surface, there is a barrier for O–O recombination ranging from 1.26 to 1.95 eV (depending on the initial O adsorption sites and the final O_2 structure). The lower value is comparable to the activation barrier obtained for the rate-limiting step of the O_2 dissociation pathway. Finally, this recombined O_2 could drive both reaction pathways.

The previous discussion leads to a picture of the water formation reaction that mostly involves the OOH formation pathway via $H_2O_2^{ad}$, but also via O–OH dissociation (with a lower probability). Moreover, the oxygen generated by the latter process might either drive the O_2 dissociation or recombine to O_2^{ad}, which could then go in both reaction pathways. This prevents the catalyst surface from being terminated by atomic oxygen.

In addition, we would like to mention a reaction step proposed by Wintterlin et al.,[59] in which the generated water desorbing from the surface continues taking part in the ongoing surface reaction by using an oxygen atom to directly form two OH^{ad} moieties [Eq. (17)]:

$$H_2O^{ad} + O^{ad} \rightarrow 2\,OH^{ad} \qquad (17)$$

This would even allow an autocatalytic mechanism for water production.

4.4. Water Solvation

We will now discuss the effects that occur if the system is solvated in water. Many experiments (such as in electrochemistry) are performed under wet conditions, and hence the presence of surrounding water molecules might change the overall energetics. Of course, for the water formation reaction there is also another motivation given by the water molecules as final reaction products: they might desorb from the surface and hydrate the system. Although sometimes results from gas-phase calculations are used to interpret the corresponding experiments performed in solution, we caution that at least some treatment of the water solvent is necessary to mimic the relevant changes.

Treatment of the surrounding water molecules explicitly within the calculated system would be most accurate, but this would require dynamic simulations of a quite extended system, which is mostly far beyond the capabilities of purely quantum-mechanical approaches. However, describing the surface and the adsorbate by DFT and modeling the solvent as a surrounding continuum shows the correct qualitative behavior.

On the basis of a self-consistent reaction field description of the water solvent, we repeated our studies on the water formation reaction. The final energetics (ΔH_f and barriers) were added to Figure 5 and highlighted in boxes. Comparison of the gas-phase and solvated systems shows a larger energy gain for the solvated system in the initial steps of depositing hydrogen and oxygen onto the surface. This is certainly due to the charge transfer between adsorbate and surface. In the case of hydrogen this results in a positive partial charge (δ^+), while each oxygen atom of adsorbed O_2 has a slightly negative partial charge (δ^-). These charges interact with the water dipoles, polarize the solvent, and thus stabilize the adsorbates. Following the O_2 dissociation pathway again a larger energy gain (0.41 eV) can be observed for the dissociation of O_2^{ad}. Since the corresponding dissociation barrier increases only from 0.65 to 0.68 eV, the larger change in ΔH_f is certainly due to the higher solvation ability of atomic oxygen compared to dioxygen. After dissociation of O_2 the adsorbed O^{ad} reacts with a surface hydrogen atom to give OH^{ad}. The energy gain with and without water solvent is almost the same (0.52 vs. 0.56 eV), whereas the energy barrier for OH formation drops drastically from 1.37 eV in the gas phase to 0.59 eV in water solution. A similar energy barrier of 0.56 eV can be observed for the following reaction step, in which OH reacts with a hydrogen atom to form water. Thus, for the O_2 dissociation pathway water solvation causes the energy barriers of the reaction steps to be quite similar (0.56, 0.59, and 0.68 eV). Instead of having the formation of OH^{ad} as the rate-limiting reaction step, the dissociation of O_2^{ad} has the highest reaction barrier, which now conforms to experimental expectations.[58]

Notably, in the water-solvated system the desorption of water from the surface requires an energy of 0.83 eV, which is comparable to the binding energy of a water molecule within an entire water bilayer network.[60–63] There the Pt–H_2O (H_2O parallel to the surface) bond energy is 0.38 eV, and each of the two hydrogen bonds formed to neighboring water molecules within the bilayer brings 0.28 eV. This adds up to a total of 0.94 eV required to remove a parallel oriented water molecule from a water bilayer network on Pt(111).[60] The results show that applying a SCRF model to the study of surface catalysis in solvating media is a reliable tool for reproducing the qualitative behavior.

Along the OOH formation pathway the initial steps are again equivalent to the O_2 dissociation, but the barrier to associate a hydrogen atom to dioxygen and form OOH increases from 0.04 eV in the gas phase to 0.40 eV in water solution. The overall energy gain for this reaction step decreases from 0.60 to 0.32 eV. Here it seems that water destabilizes the transition state Pt–(OO–H) and final state Pt–OOH of this process, which also explains the 0.12 eV lower energy barrier for the following O–OH dissociation. During the latter reaction step the system energy lowers by 1.94 eV, which is 0.72 eV more than in the gas phase. The final step of forming water out of OH^{ad} and H^{ad} is again equivalent to the O_2 dissociation pathway.

However, if OOH^{ad} is not being dissociated to OH and O directly, but is once more hydrogenated to $H_2O_2^{ad}$, the system has to overcome an even higher barrier of 0.94 eV, which is 0.47 eV higher than in the gas phase. On comparing the increases in the reaction barriers caused by the solvent for the

formation of OOH and H_2O_2, we observe comparable values (0.36 and 0.47 eV). Thus, it seems that for both OOH and H_2O_2 the surface bond is weakened by a similar amount.

In contrast to the gas-phase OOH formation pathway, where we found that the mechanism via $H_2O_2^{ad}$ involved the lowest energy barrier and therefore was more likely to occur, inclusion of the water solvent changes this behavior. Now the mechanism that directly dissociates OOH^{ad} has a 0.32 eV lower barrier and seems to be the preferred process.

By comparing the energy barriers of the various reaction steps in both pathways (not considering the process via H_2O_2), it seems that solvating the system equilibrates all barriers to be within a range of 0.40 to 0.62 eV. Therefore, different from the gas-phase system, where we found a strong preference for the OOH formation pathway, both the O_2 dissociation and the OOH formation processes are likely to occur with comparable probabilities. In particular, since both reaction pathways produce adsorbed atomic oxygen as well as water, but only the O_2 dissociation pathway uses these within the reaction cycle, the reaction rate for the latter pathway increases.

Overall, starting with H_2^{aq} and O_2^{aq} the whole system gains 4.38 eV while reacting to give $H_2O^{g,aq}$ and fcc-adsorbed atomic oxygen. Subtracting $\Delta H_f(O^{ad}_{fcc})$ from this value gives $4.38-1.67=2.71$ eV, which should be compared to the tabulated enthalpy value of 2.96 eV for the reaction $H_2^{aq}+{}^1/_2\,O_2^{aq}\rightarrow H_2O^{aq}$. The remaining difference of 0.25 eV can be rationalized as follows. For a single solvated H_2O^{aq} molecule we obtain a heat of formation of 2.89 eV (exp.: 2.96 eV), and thus the difference of 0.25 eV comes from simulating the solvated surface with a continuum approach. However, the solvated surface contributes to all energy values, assuming that error cancellation for energy differences is a reasonable assumption.

Within this section we have shown how crucially the effects introduced by solvating the system in water could affect the energetics of each reaction step, and finally the preferred reaction mechanism. Using the results obtained for the gas-phase system to interpret a solvated system would have been misleading here.

5. Pt-Based Alloys

We would now like to discuss the effects that might occur by not using a pure catalyst, but a heterogeneous mixture of two metals (alloys). As systems we compare pure Pt and Pt/Ni alloys with the same (111) surface plane. Since Pt and Ni have different electronic properties, alloying could result in changes of the surface structure by relaxation or even reconstruction. While relaxation only includes deviations of the layer distance from the corresponding bulk value, reconstructions can even involve atom displacements, which could lead to totally different surfaces. If the system is heated to temperatures where the kinetic barriers of atom displacements within the alloy might be overcome, segregation could occur. There, the system lowers its energy (surface energy) by accumulating one of the two species at the surface.

Experimentally different Pt/Ni alloy crystal structures (compositions) have been studied ($Pt_{0.1}Ni_{0.9}$, $Pt_{0.25}Ni_{0.75}$, $Pt_{0.5}Ni_{0.5}$, and $Pt_{0.78}Ni_{0.22}$) using low-energy electron diffraction (LEED), X-ray photoelectron spectroscopy (XPS), and medium-energy ion scattering (MEIS).[64,65] While the bulk structure forms fcc solid solutions over the whole range of compositions, Bardi et al. studied the (111) surface of a comparable alloy, Pt_3Co, and found that on the surface an ordered fcc-like structure forms first, which under UHV treatment shows segregation of Pt toward the surface.[66] In the case of $Pt_{0.78}Ni_{0.22}$(111), which should be of particular interest here, this finally results in a first surface layer consisting of Pt only, while the next three layers have a damped oscillatory Pt/Ni composition profile.[67] Beginning with the fourth layer the system has the expected 3:1 bulk mixture of Pt_3Ni.

In the following discussion we first reproduce the surface segregation effects on the basis of periodic DFT calculations, and then study the changes that can be expected by not using semi-infinite alloy surfaces, but highly dispersed alloy particles as catalyst.

5.1. Extended Surface

As already mentioned, some of the Pt-based alloys show strong surface segregations. To study this effect on the quantum-mechanical level, we focused on Pt/Ni alloys and first calculated the corresponding bulk structure. On the basis of periodic DFT calculations[41,42] (for further information see ref. [50]) an fcc-like bulk unit cell with Pt atoms at the faces and Ni atoms at the corners gave a lattice constant a_0 of 3.89 Å. This unit cell conforms to the crystal structures of pure Pt ($a_0=$ 3.92 Å) or Ni ($a_0=3.52$ Å) and leads to a Pt_3Ni bulk composition. In addition, for the Pt_3Ni alloy crystal we obtained a cohesive energy of $E_{coh}(Pt_3Ni)=22.63$ eV, which can be compared to the experimental values for pure Pt ($E_{coh}(Pt_4)=23.36$ eV) and pure Ni ($E_{coh}(Ni_4)=17.76$ eV).[68] A comparison of the lattice constants and cohesive energies indicates the domination of Pt.

Using the calculated lattice constant for Pt_3Ni, segregation on the (111) surface was studied by a series of periodic DFT calculations on systems with different Pt:Ni ratios and compositions. Besides changing the composition, for each number of Pt and Ni atoms various possible site distributions were considered, too. As surface models we used slab geometries (five layers) with either 2×2 or 2×3 unit cells, in which the lowest two surface layers were fixed at the corresponding bulk layer distance. Among the different systems that have been studied, Figure 6 shows the most stable (top left) and some of the more stable 2×3 structures. Restricted to the variations that 2×2 and 2×3 unit cells allow, we find that having a distribution of 100% Pt in the first, 50% in the second, and 83% Pt in the third layer gives the highest binding energy and results in the most stable structure. These distributions should be compared to the experimental values[68] for $Pt_{0.78}Ni_{0.22}$ of 99, 30, and 87%, which is in excellent agreement with our calculations.

Besides the surface segregation we can also compare the distances between the surface layers. Here LEED experiments[68] on $Pt_{0.78}Ni_{0.22}$ give 2.18 ± 0.02 Å as the distance between the first three surface layers and 2.220 Å as the bulk layer distance. As shown in Figure 6, we obtain a range of 2.11

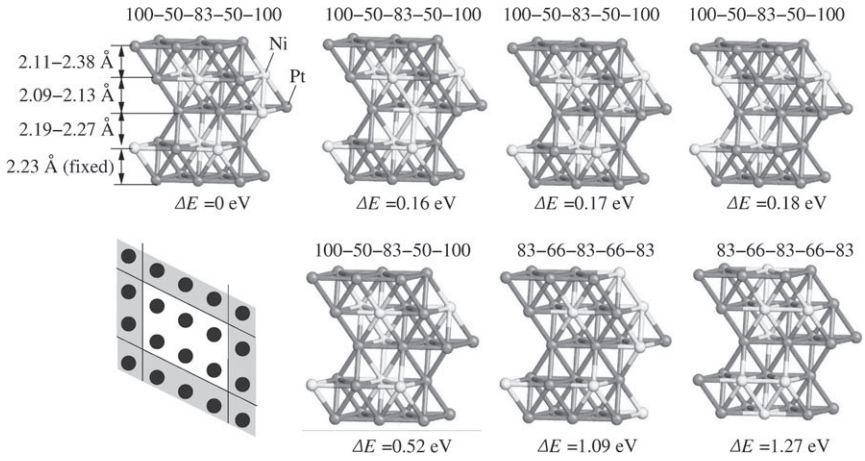

Figure 6. Various 2×3 unit cells calculated to study surface segregation in Pt_3Ni. The number above each structure gives the amount of Pt in each layer [%], while the energies below are the differences in total energy with respect to the most stable structure. In addition, layer distances are given for the most stable structure.

to 2.38 Å for the distance between the first and second surface layers. This difference is due to the shorter Pt–Ni surface bond, which causes a slight buckling of the top Pt layer. However, the average distance of 2.24 Å compares well to the experimental value. The same holds true for the distance between the second and third atomic layers. Here, again due to the variations in bond length, our values range from 2.09 to 2.13 Å. Finally, for the bulk layer distance we calculated 2.23 Å, which is in perfect agreement with the experimental value mentioned before.

Although the changes in the electronic structure and therefore the chemical behavior of extended alloy surfaces are interesting by themselves, and much has been done from the experimental[69,70] and theoretical[71–73] side, many experimental or industrial applications use highly dispersed catalysts rather than semi-infinite surfaces. This usually provides a larger surface area, where the catalytic reaction can run simultaneously and results in higher efficiencies. The size of these catalyst particles might range from <1 to 5 nm in diameter. Thus, it is questionable whether the effects occurring on extended surfaces can be observed on such nanoparticles, too.

5.2. Nanoparticles

Equivalent to the procedure applied to study surface segregation on semi-infinite systems, to extend those considerations to nanoparticles requires calculations on the stability of differently sized and shaped clusters with varying Pt:Ni ratios and compositions. Compared to the cluster-convergence studies described in Section 3, where systems with less than 20 atoms showed an unpredictable behavior, we expect even larger particles to be required to model alloy surfaces. Moreover, since the relative surface area of small particles is much larger than that of semi-infinite surfaces, we also expect structural deviations.

In a series of DFT calculations on different clusters, we studied the preferred structure for Pt/Ni particles up to 35 atoms containing Pt and Ni in different amounts and compositions.[50] It turned out that for small single-layer particles Ni prefers to coordinate to six Pt atoms and minimizes the number of direct Ni–Ni bonds. This finding can be understood in terms of an average Pt–Ni bond being 0.80 eV stronger than a Ni–Ni bond. It leads to a bulklike structure where every Ni atom is surrounded by six Pt atoms, which results in a 3:1 ratio between Pt and Ni. Consequently, those Ni atoms that are located at edges try to coordinate to four Pt atoms.

As concerns the electronic structure of the single-layer alloy particles, the spin density and charge distribution analyses suggest an $s^{0.35}d^{8.75}$ configuration for each Ni atom, while all Pt atoms have $s^{0.89}d^{9.41}$ character. Comparison of these values with those obtained for pure Pt clusters ($s^{0.83}d^{9.17}$) indicates a reduction of unpaired spins on each Pt atom of the Pt/Ni alloy, which consequently leads to lower binding energies of adsorbates (see Section 5.3).

The introduction of a second layer to the clusters does not change the preference for a bulklike Pt/Ni distribution. In their most stable geometries each Ni atom tries to be sixfold coordinated to Pt atoms and thus maximize the number of Pt–Ni bonds, while avoiding Ni–Ni bonds. Although an average Pt–Pt bond is slightly stronger than a Pt–Ni bond, the energy loss by having two Ni atoms at adjacent lattice sites would lead to an overall lower stability.

For three-layer clusters, which besides two surface layers (top and bottom) start to develop some volume layer, we also see a structure where each Ni atom tries to connect to Pt atoms, which results again in the bulklike structure. However, since the various surface faces of a cluster are finite, the bulklike structure can be achieved with a slight Pt or Ni enrichment at the surface. In the present case the clusters show a slight Pt enrichment at the (111) faces, which might indicate the beginning of surface segregation. However, a three-layer cluster with 35 atoms is still far away from a semi-infinite surface.

To summarize, it turned out that Pt/Ni nanoparticles even up to 35 atoms ($\approx$1.5 nm in diameter) do not show the expected surface segregation known for extended surfaces. Instead, due to the ratio between atoms at the surface and in the volume (three-layer clusters still do not allow one to speak of "bulk" atoms), nanoparticles show a bulklike composition over the entire system. For the theoretical modeling this has two consequences:

- In cases when experiments on extended alloy surfaces are simulated, small clusters are not able to reproduce the correct surface structure. Thus, periodic approaches, such as using slabs, should be applied.

- If highly dispersed alloy particles are used to catalyze a reaction, they might have surface compositions that significantly differ from those of their semi-infinite surface analogs. To simulate such systems, careful particle-size and-shape dependent studies on the alloy composition are required prior to simulating the catalytic reaction.

In the following we will study the electronic structure at the (111) surface of a three-layer 35-atom Pt/Ni alloy cluster (see Figure 7) and compare it to that of a pure Pt system. First, this

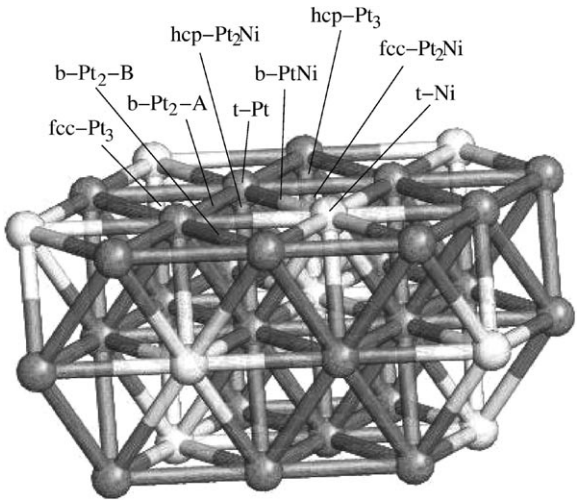

Figure 7. The 35-atom cluster ($Pt_{10.10.6}Ni_{4.3.2}$) used in the study of the surface electronic structure of alloy nanoparticles. The labels indicate all possible sites for adsorption, and distinguish between the local environment by second-layer atoms.

will show how an alloy particle might behave in a catalytic reaction, and second, this should mimic the surface experiments by Paulus et al. that employed well-prepared (by a series of sputtering and annealing cycles) $Pt_3Ni(111)$ surfaces and found an enhanced rate for oxygen reduction.[74]

5.3. Surface Electronic Structure

To study the surface electronic structure of catalytic Pt/Ni alloy particles, we calculated the adsorption of atomic hydrogen and oxygen on all distinguishable surface sites (see ref. [50] for further details). This choice is motivated by hydrogen being more electropositive than Pt and oxygen more electronegative. Thus, these two atoms should allow us to draw a qualitative picture on how the adsorption of different species might be influenced by alloying the metal. In addition, in Section 4 we have seen that OH formation is one of the crucial reactions steps in the formation of water on Pt(111). Therefore, the study of these two adsorbates could provide a deeper insight into the origin of the enhanced rate for oxygen reduction (ORR) found experimentally with these alloys[74] and other Pt-based alloys.[75–79]

Compared to the homoatomic system, where the (111) surface has four different adsorption positions, the Pt/Ni(111) alloy surface has nine distinguishable sites (Figure 7). During the calculations it turned out that the type of neighboring atom in the second layer also strongly influences the binding energy (see below). The adsorption of H or O atoms on pure Pt(111) or Pt/Ni(111) led to the same changes in the ground spin state of the system. Thus, in both cases the adsorbates form covalent bonds to the surface d orbitals, while the number of bonds is determined by the valence electrons of the adsorbate. However, due the presence of Ni atoms the binding energies at different surface sites, which are summarized in Table 2, show larger fluctuations than on pure Pt. This finding is also summarized in the two contour plots shown in Figure 8.

Table 2. Binding energies and vibration frequencies for the adsorption of atomic hydrogen and oxygen on Pt(111) (represented by the $Pt_{14.13.8}$ cluster) and on Pt/Ni(111) (represented by the $Pt_{10.10.6}Ni_{4.3.2}$ cluster). In each system the adsorbate and the central four Pt atoms of the first layer (relaxation effects) were fully geometry-optimized.

System	Adsorption site	E_{bind} [eV]	Vibration frequency [cm^{-1}]
$Pt_{14.13.8}$–H	top	2.661	2456
	bridge	2.607	1317
	hcp	2.489	
	fcc	2.618	
$Pt_{14.13.8}$–O	top	2.098	
	bridge	2.789	531
	hcp	3.026	510
	fcc	3.370	
$Pt_{10.10.6}Ni_{4.3.2}$–H	t-Ni	1.782	1917
	t-Pt	2.673	2319
	b-PtNi	2.598	1450
	b-Pt_2 -A	2.411	1337
	b-Pt_2 -B	2.483	1522
	fcc-Pt_2Ni	2.551	1750
	hcp-Pt_2Ni	2.356	1205
	fcc-Pt_3	2.198	1296
	hcp-Pt_3	2.269	1158
$Pt_{10.10.6}Ni_{4.3.2}$–O	t-Ni	1.639	970
	t-Pt	1.834	746
	b-PtNi	2.976	649
	b-Pt_2 -A	2.456	970
	b-Pt_2 -B	3.270	902
	fcc-Pt_2Ni	3.501	910
	hcp-Pt_2Ni	3.413	967
	fcc-Pt_3	2.327	866
	hcp-Pt_3	3.302	707

On Pt(111) oxygen binds most strongly to an fcc site (3.37 eV), while on the alloy particles fcc-Pt_2Ni leads to the highest binding energy (3.50 eV). The latter surface site is a threefold position formed by two Pt atoms and one Ni atom. In contrast, on Pt(111) the weakest oxygen binding was obtained on top of a Pt atom (2.10 eV), which on the alloy surface is on top of a Ni atom (1.64 eV). As regards the oxygen surface diffusion, there is a relatively small barrier of 0.23 eV for the atom to hop between the two adjacent triangles marked in Figure 8. However, long-range diffusion is determined by a larger barrier of 0.56 eV, which is comparable to the energy barrier of 0.58 eV obtained for pure Pt(111).

Even more significant changes appear with hydrogen. On a pure Pt(111) surface the small diffusion barrier of $\approx$0.05 eV

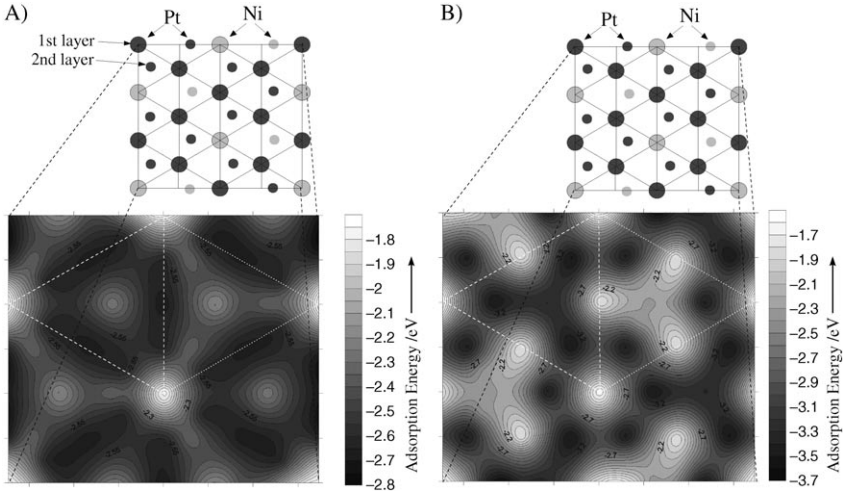

Figure 8. Contour plots for the binding energy of atomic H (A) and atomic O (B) on the $Pt_3Ni(111)$ surface. Dark areas indicate strong surface binding. Hydrogen prefers to bind on top of a Pt atom, while oxygen prefers an fcc-Pt_2Ni site with no atom beneath in the second layer.

leads to quite mobile surface hydrogen, while adsorption energies on Pt/Ni(111) vary between 1.78 and 2.67 eV. This leads to a net diffusion barrier of 0.26 eV, which is around five times as high as that on pure Pt. However, similar to oxygen, the barrier to hop between the two triangles marked in Figure 8 is lower (0.12 eV).

Summarizing the results for both oxygen and hydrogen, as representatives of charge-donating and -accepting adsorbates, shows a more structured potential energy surface for binding on the alloy surface than on pure Pt. This leads to a higher localization of the adsorbates, which in case of oxygen and hydrogen is restricted to the triangles formed by surface Ni atoms. In addition, the preferred surface locations of oxygen and hydrogen show a strong overlap. Both these aspects might play a role in enhancing the rate for the overall oxygen reduction reaction. However, to fully answer this question would require further considerations comparable to those described in Section 4.

6. Conclusions

Heterogeneous catalysis has been a subject of research for almost 200 years, but the enormous variety of possible surface reactions still reveal many open questions regarding the exact reaction pathways, kinetics, or structural information. For example, the seemingly simple reaction of forming water out of H_2 and O_2 over a Pt catalyst shows many different reaction pathways. In addition, changes in the environment (e.g. solvation) result in sometimes drastically modified reaction mechanisms and overall kinetics. Thus, an accurate theoretical modeling of catalysis requires comprehensive studies that take environmental effects into account. Moreover, in recent times alloying metal surfaces or using nanoparticles rather than extended surfaces has become increasingly of interest. Both aspects offer a whole variety of new catalyst materials with modified properties. In these fields especially, where atom-resolved information is difficult to extract experimentally, theoretical simulations become rather important in understanding the underlying processes on the atomic scale.

Acknowledgements

T.J. gratefully acknowledges support by the German academic exchange service (DAAD) and the Fond der Chemischen Industrie (VCI).

Keywords: catalysis · density functional calculations · platinum · surface chemistry · water chemistry

[1] G. A. Somorjai in *Introduction to Surface Chemistry and Catalysis*, J. Wiley & Sons Inc., New York, **1994**.
[2] P. A. Dowben, A. Miller in *Surface Segregation Phenomena*, CRC Press, Boca Raton, **1990**.
[3] W. Vielstich, H. A. Gasteiger, A. Lamm in *Handbook of Fuel Cells—Fundamentals, Technology, and Application, Vol. 1: Fundamentals and Survey of Systems*, J. Wiley & Sons Ltd., West Sussex, **2003**.
[4] C. L. Haynes, A. D. McFarland, M. T. Smith, J. C. Hulteen, R. P. van Duyne, *J. Phys. Chem. B* **2002**, *106*, 1898 – 1902.
[5] E. Hao, G. C. Schatz, J. T. Hupp, *J. Fluoresc.* **2004**, *14*, 331 – 341.
[6] D. R. Hartree, *Proc. Camb. Philos. Soc.* **1928**, *24*, 89 – 110.
[7] V. A. Fock, *Z. Phys.* **1930**, *15*, 126.
[8] P. Hohenberg, W. Kohn, *Phys. Rev.* **1964**, *136*, B864.
[9] W. Kohn, L. J. Sham, *Phys. Rev.* **1965**, *140*, A1133.
[10] M. Weinert, E. Wimmer, A. J. Freeman, *Phys. Rev. B* **1982**, *26*, 4571 – 4578.
[11] B. G. Johnson, P. M. W. Gill, J. A. Pople, *J. Chem. Phys.* **1993**, *98*, 5612 – 5626.
[12] C. Fiolhais, F. Nogueira, M. Marques in *A Primer in Density Functional Theory*, Springer, Berlin, **2003**.
[13] A. D. Becke, *J. Chem. Phys.* **1993**, *98*, 5648 – 5652.
[14] C. Lee, W. Yang, R. G. Carr, *Phys. Rev. B* **1988**, *37*, 785 – 789.
[15] N. L. Allinger, Y. H. Yuh, J.-H. Lii, *J. Am. Chem. Soc.* **1989**, *111*, 8551 – 8566.
[16] N. L. Allinger, F. Li, L. Yan, *J. Comput. Chem.* **1990**, *11*, 848 – 867.
[17] S. L. Mayo, B. D. Olafson, W. A. Goddard III, *J. Phys. Chem.* **1990**, *94*, 8897 – 8909.
[18] A. K. Rappé, C. J. Casewit, K. S. Colwell, W. A. Goddard III, W. M. Skiff, *J. Am. Chem. Soc.* **1992**, *114*, 10024 – 10035.
[19] G. C. Abell, *Phys. Rev. B* **1985**, *31*, 6184 – 6196.
[20] J. Tersoff, *Phys. Rev. B* **1989**, *39*, 5566 – 5568.
[21] A. C. T. van Duin, S. Dasgupta, F. Lorant, W. A. Goddard III, *J. Phys. Chem. A* **2001**, *105*, 9396 – 9409.
[22] A. C. T. van Duin, A. Strachan, S. Stewman, Q. Zhang, X. Xu, W. A. Goddard III, *J. Phys. Chem. A* **2003**, *107*, 3803 – 3811.
[23] T. Jacob, A. C. T. van Duin, W. A. Goddard III, unpublished results.
[24] J. Gao, *Acc. Chem. Res.* **1996**, *29*, 298 – 305.
[25] J. Gao, *Rev. Comput. Chem.* **1996**, *7*, 119 – 185.
[26] R. Car, M. Parrinello, *Phys. Rev. Lett.* **1985**, *55*, 2471 – 2474.
[27] M. J. Field, P. A. Bash, M. Karplus, *J. Comput. Chem.* **1990**, *11*, 700 – 733.
[28] J. Gao, X. Xia, *Science* **1992**, *258*, 631 – 635.
[29] M. Dupuis, G. K. Schenter, B. G. Garrett, E. E. Arcia, *Theochem* **2003**, *632*, 173 – 183.
[30] J. Gao, *J. Phys. Chem.* **1992**, *96*, 537 – 540.
[31] N. W. Moriarty, G. Karlstrom, *J. Phys. Chem.* **1996**, *100*, 17791 – 17796.
[32] N. W. Moriarty, G. Karlstrom, *J. Chem. Phys.* **1997**, *106*, 6470 – 6474.
[33] J. Tomasi, M. Persico, *Chem. Rev.* **1994**, *94*, 2027 – 2094.
[34] C. J. Cramer, D. G. Truhlar, *Chem. Rev.* **1999**, *99*, 2161 – 2200.
[35] M. Cossi, B. Mennucci, R. Cammi, *J. Comput. Chem.* **1996**, *17*, 57 – 73.
[36] M. F. Sanner, A. J. Olson, J. C. Spehner, *Biopolymers* **1996**, *38*, 305 – 320.
[37] D. Eisenberg, A. D. McLachlan, *Nature* **1986**, *319*, 199 – 203.

[38] W. C. Still, A. Tempczyk, R. C. Hawley, T. Hendrickson, *J. Am. Chem. Soc.* **1990**, *112*, 6127 – 6129.
[39] D. Qiu, P. S. Shenklin, F. P. Hollinger, W. C. Still, *J. Phys. Chem. A* **1997**, *101*, 3005 – 3014.
[40] K. Horn, M. Scheffler in *Handbook of Surface Science Vol. 2: Electronic Structure*, Elsevier, Amsterdam, **2000**.
[41] P. A. Schultz, unpublished results; a description of the method is in: P. J. Feibelman, *Phys. Rev. B* **1987**, *35*, 2626 – 2646.
[42] C. Verdozzi, P. A. Schultz, R. Wu, A. H. Edwards, N. Kioussis, *Phys. Rev. B* **2002**, *66*, 125408.
[43] J. P. Perdew, K. Burke, M. Ernzerhof, *Phys. Rev. Lett.* **1996**, *77*, 3865 – 3868.
[44] T. Jacob, R. P. Muller, W. A. Goddard III, *J. Phys. Chem. B* **2003**, *107*, 9465 – 9476.
[45] T. Jacob, J. Anton, S. Fritzche, W.-D. Sepp, B. Fricke, *Phys. Lett. A* **2002**, *300*, 71 – 75.
[46] T. Jacob, D. Geschke, S. Fritzsche, W.-D. Sepp, B. Fricke, J. Anton, S. Varga, *Surf. Sci.* **2001**, *486*, 194 – 202.
[47] H. Gerischer, C. W. Tobias in *Advances in Electrochemistry and Electrochemical Engineering*, J. Wiley & Sons Inc., New York, **1984**.
[48] T. Jacob, unpublished results.
[49] Ş. C. Bădescu, P. Salo, T. Ala-Nissila, S. C. Ying, K. Jacobi, Y. Wang, K. Bedürftig, G. Ertl, *Phys. Rev. Lett.* **2002**, *88*, 136 101.
[50] T. Jacob, W. A. Goddard III, *J. Phys. Chem. B* **2004**, *108*, 8311 – 8323.
[51] A. Eichler, F. Mittendorfer, J. Hafner, *Phys. Rev. B* **2000**, *62*, 4744 – 4755.
[52] B. C. Stipe, M. A. Rezaei, W. Ho. , S. Gao, M. Persson, B. I. Lundquist, *Phys. Rev. Lett.* **1997**, *78*, 4410 – 4413.
[53] W. Ho, *Science* **1998**, *279*, 1907 – 1909.
[54] W. Ho, *Acc. Chem. Res.* **1998**, *31*, 567 – 573.
[55] D. H. Parker, M. E. Bartram, B. E. Koel, *Surf. Sci.* **1989**, *217*, 489 – 510.
[56] P. A. Thiel, T. E. Madey, *Surf. Sci. Rep.* **1987**, *7*, 211 – 385.
[57] W. Vielstich, H. A. Gasteiger, A. Lamm in *Handbook of Fuel Cells—Fundamentals, Technology, and Application, Vol. 2: Electrocatalysis*, J. Wiley & Sons Ltd., West Sussex, **2003**.
[58] R. A. Olsen, G. J. Kroes, E. J. Baerends, *J. Chem. Phys.* **1999**, *111*, 11155 – 11163.
[59] C. Sachs, M. Hildebrand, S. Völkening, J. Wintterlin, G. Ertl, *J. Chem. Phys.* **2002**, *116*, 5759 – 5773.
[60] T. Jacob, W. A. Goddard III, *J. Am. Chem. Soc.* **2003**, *126*, 9360 – 9368.
[61] S. Meng, L. F. Xu, E. G. Wang, S. Gao, *Phys. Rev. Lett.* **2002**, *89*, 176 104.
[62] B. Ruscic, A. F. Wagner, L. B. Harding, R. L. Asher, D. Feller, D. A. Dixon, K. A. Peterson, Y. Song, X. M. Qian, C. Y. Ng, J. B. Liu, W. W. Chen, *J. Phys. Chem. A* **2002**, *106*, 2727 – 2747.
[63] O. Ogasawara, B. Brena, D. Nordlund, M. Nyberg, A. Pelmenschikov, L. G. M. Petterson, A. Nilsson, *Phys. Rev. Lett.* **2002**, *89*, 276 102.
[64] M. A. Vasiliev, *J. Phys. D* **1997**, *30*, 3037 – 3070.
[65] M. Lundberg, *Phys. Rev. B* **1987**, *36*, 4692 – 4699.
[66] U. Bardi, B. C. Beard, P. N. Ross, *J. Catal.* **1990**, *124*, 22 – 29.
[67] Y. Gauthier, Y. Joly, R. Baudoing, J. Rundgren, *Phys. Rev. B* **1985**, *31*, 6216 – 6218.
[68] Ch. Kittel in *Einführung in die Festkörperphysik*, R. Oldenbourg Verlag, München, **1991**.
[69] D. P. Woodruff in *Surface Alloys and Alloy Surfaces*, Elsevier Science, The Netherlands, **2002**.
[70] A. Mookerjee, D. D. Sarma in *Advances in Condensed Matter Science Vol. 4: Electronic Structure of Alloys, Surfaces and Clusters*, CRC Press, **2002**.
[71] J. Greeley, J. K. Nørskov, *Surf. Sci.* **2005**, *592*, 104 – 111.
[72] H. Toulhoat, P. Raybaud, *J. Catal.* **2003**, *216*, 63 – 72.
[73] C. J. H. Jacobsen, S. Dahl, B. S. Clausen, S. Bahn, A. Logadottir, J. K. Nørskov, *J. Am. Chem. Soc.* **2001**, *123*, 8404 – 8405.
[74] U. A. Paulus, A. Wokaun, G. G. Scherer, T. J. Schmidt, V. Stamenković, N. M. Marković, P. N. Ross, *Electrochim. Acta* **2002**, *47*, 3787 – 3798.
[75] B. C. Beard, P. N. Ross, *J. Electrochem. Soc.* **1990**, *137*, 3368 – 3374.
[76] J. T. Glass, G. L. Cahen, G. E. Stoner, F. J. Taylor, *J. Electrochem. Soc.* **1987**, *134*, 58 – 65.
[77] M. Min, J. Cho, K. Cho, H. Kim, *Electrochim. Acta* **2000**, *45*, 4211 – 4217.
[78] G. Tamizhmani, G. A. Capuano, *J. Electrochem. Soc.* **1994**, *141*, 968 – 975.
[79] V. Stamenković, T. J. Schmidt, P. N. Ross, N. M. Marković, *J. Chem. Phys. B* **2002**, *106*, 11 970 – 11 979.

Received: November 9, 2005
Revised: December 12, 2005
Published online on April 5, 2006

